Superlattice-induced oscillations of interplanar distances and strain effects in the CrN/AlN system

Zaoli Zhang,[1,*] Xunlong Gu,[1,2] David Holec,[3] Matthias Bartosik,[4] Paul H. Mayrhofer,[4] and H. P. Duan[2]
[1]*Erich Schmid Institute of Materials Science, Austrian Academy of Sciences, Leoben, Austria*
[2]*School of Materials Science and Engineering, Beihang University, Beijing 100083, People's Republic of China*
[3]*Department of Physical Metallurgy and Materials Testing, Montanuniversität Leoben, Austria*
[4]*Institute of Materials Science and Technology, TU Wien, A-1060 Vienna, Austria*
(Received 13 January 2017; published 5 April 2017)

New physical phenomena and exciting material properties may be introduced by interfaces present in multilayers. Here, interplanar spacing oscillations in cubic CrN/AlN multilayers were experimentally observed by using spherical aberration-corrected high-resolution transmission electron microscopy, and corroborated by first-principles calculations. These oscillations are closely related to changes in the electronic structure. Electron spectroscopy and microscopy were employed to obtain generalized relationships between the electronic structure on the one hand, and (non-)stoichiometry or strains in the strained multilayers on the other hand, which are successfully interpreted by means of theoretical calculations. The present study may provide atomic-scale clues on the mechanism of extraordinary strength pertaining to the CrN/AlN multilayers.

DOI: 10.1103/PhysRevB.95.155305

I. INTRODUCTION

Designing new materials by taking advantage of nonequilibrium (metastable) phases via their epitaxial stabilization or obtained by combining some attractive properties of different elements has always been an exciting challenge of modern materials physics. A multilayer architecture, which comprises a periodic alternation of chemically and/or structurally different layers, is one of the most versatile and promising approaches with respect to properties and performance, hence finding a large variety of applications such as optical, magnetic, electronic, and mechanical or tribological, e.g., nanoscale multilayered hard coatings [1–8]. Properties of the metastable phase are often unknown, which makes it difficult to apply knowledge-based property-targeted optimization of such multilayers. The most prominent example from the field of hard coatings is *Me*N/AlN (Me = Ti,V,Cr); among them, the AlN/CrN multilayers have received the most attention, and have been studied both experimentally and theoretically [9–11]. It was experimentally and theoretically found that a nonequilibrium rocksalt-type *cubic* AlN metastable phase forms by epitaxial growth onto *fcc Me*N when the AlN layer thickness is sufficiently thin (e.g., $\leqslant$4 nm) via an epitaxial stabilization effect [12–17]; for thicker AlN layer thickness, AlN crystallizes in its thermodynamically stable wurtzite structure.

Epitaxial stabilization of nonequilibrium structures in thin layers has been applied to nitride hard-coating materials, and designs a new class of multilayers for electronics [8]; however, the physical mechanism and consequences of the epitaxial stabilization are not yet well understood due to the complexity of the multilayer films in different systems, and rather limited atomic-resolution studies of the interface structure and composition performed to date. To reveal the intrinsic physics pertaining to the multilayers is a key to understand their unique properties and to design novel multilayered materials.

Transition electron microscopes (TEMs) equipped with a spherical aberration (C_S) correction technique allow characterizing with atomic resolution and hence observation of very localized atoms, e.g., at the interface and defects [18,19]. This in turn sheds light on the atomic and electronic structure variations in the nanolayered materials, and thus provides access to the very origins of many extraordinary properties, e.g., hardness enhancement in multilayered films, and uncovers the atomic mechanism of epitaxial stabilization [11,20]. We therefore combine atomic-resolution imaging, quantitative measurements, and atomic-resolution EELS (electron-energy-loss spectroscopy) analyses and ELNES (electron-energy-loss near-edge structure) in TEM and complement them with first-principles calculations.

II. METHODS

CrN/AlN multilayer films were deposited on single-crystal Si (100) substrates by means of unbalanced magnetron sputtering using Cr (99.9% purity) and Al (99.9% purity) targets [21]. The target power for both Cr and Al was 250 W. The sputtering was conducted in an Ar-N_2 gas mixture with a total pressure of 0.4 Pa and N_2 partial pressure of 0.24 Pa. The bias voltage and temperature of substrates during deposition were -70 V and 470 °C, respectively.

A JEOL 2100F field-emission microscope (200 kV) equipped with an image-side C_S corrector which possesses a 1.2-Å resolution at 200 kV was used. Scanning TEM (STEM) images shown here were recorded using an annular STEM detector, with the detector inner angle/outer angle set to around 54 mrad/144 mrad. Under these conditions, a STEM high-angle annular dark-field image is a nearly Z-contrast image. STEM-EELS spectrum images were acquired using a dispersion of 0.2 eV/channel, a collection semiangle of 10 mrad, and a convergence semiangle of 7.5 mrad. The probe size under optimum conditions can be as small as 0.2 nm (the actual size could be larger, i.e., about 0.5–1.0 nm). For the EELS spectrum images, the following procedure was performed. First, multivariate statistical analysis was applied to the raw data of all spectrum images. Second, the background

*zaoli.zhang@oeaw.ac.at

for each spectrum was removed using a power-law function, and Hartree-Slater models were used to fit the L_2 and L_3 edges. The cross sections were then subtracted within the signal window of 569.4–577.4 eV for Cr-L_3 and of 578–586 eV Cr-L_2, respectively. To quantify the atomic ratio of Cr/N, the energy windows for background subtraction were set to 80 and 130 eV, and signal windows were set to 120 and 130 eV for Cr and N, respectively.

Prior to quantitative measurements, the high-resolution TEM (HRTEM) images were carefully calibrated using Si substrate. A peak fitting using Gaussian function based on the HRTEM image was applied to refine the center of maximum of atomic column position for determining the interplanar spacings. The approach was justified by achieving a residual intensity minimum (i.e., less than 1%).

Density functional theory (DFT) calculations as implemented in the plane-wave pseudopotential Vienna Ab initio Simulation Package (VASP) [22,23] were performed. Supercells were constructed by stacking equal numbers of 16-atom building blocks of AlN and CrN on top of each other. Each of these building blocks is a $2 \times 2 \times 1$ supercell of $[\frac{1}{2}\ -\frac{1}{2}\ 0] \times [\frac{1}{2}\ \frac{1}{2}\ 0] \times [0\ 0\ 1]$ cell of the eight-atom conventional cubic cell. In total, we have considered three supercell sizes: two building blocks of AlN and two building blocks of CrN denoted as 2+2 and having a bilayer period $\Lambda = 1.6$ nm and consisting of 64 atoms (16 Cr, 16 Al, 32 N), a 3+3 supercell with $\Lambda = 2.4$ nm (24 Cr, 24 Al, 48 N), and a 4+4 supercell with $\Lambda = 3.2$ nm (32 Cr, 32 Al, 64 N). Magnetic spins up and down on Cr atoms were distributed according to a special quasirandom structures method [24] for quasibinary materials, hence to approximate the paramagnetic state with collinear disordered local magnetic moments [9,25,26]. The plane-wave cutoff energy was set to 700 eV and the Brillouin zone was sampled with $6 \times 6 \times 2$, $6 \times 6 \times 2$, and $6 \times 6 \times 1$ k points for the 2+2, 3+3, and 4+4 supercell, respectively. The electron-electron interactions were described within the generalized gradient approximation as parametrized by Perdew *et al.* [27], while projector-augmented method-capable pseudopotentials [28] were employed for describing the electron-ion interaction. All supercells were fully optimized with respect to volume, cell shape, and atomic positions until the forces on atoms were below 0.01 eV/Å. The N-K-edge ELNES of AlN was calculated using an all-electron WIEN2K code [29] allowing for a straightforward implementation of the Slater transition state via a core-hole approach [30]. The core-hole calculations were performed using a 64-atom supercell ($2 \times 2 \times 2$ conventional cubic $B1$ structure), and by placing a ½ 1s core electron into the background charge [30,31]. The total number of 500 K points in the whole Brillouin zone, muffin-tin radii of 1.96 bohrs (Al) and 1.86 bohrs (N), and $R_{\mathrm{MT}}k_{\max} = 7$ were applied. The VESTA package [32] was used for visualization of the structures.

III. RESULTS AND DISCUSSION

A. HRTEM quantitative measurements

By HRTEM quantitative measurement utilizing the Gaussian function fitting approach, the interplanar distances in a direction perpendicular to interfaces (i.e., in the growth direction) were determined. Here, atomic displacement measurements were carried out on a multilayer with a bilayer period of $\Lambda = 6.0$ nm. A representative HRTEM image and corresponding interplanar spacing variations over several layers (Fig. 1) reveal an interesting trend: The interplanar spacings oscillate in the CrN layers while no such sawlike behavior is observed in the AlN layers. Moreover, the spacings in AlN are smaller than in CrN, which can be understood from the fact that AlN has a smaller lattice constant (4.05 Å) than CrN (4.13 Å), and hence the epitaxial relationship causes in-plane tension in AlN and a corresponding Poisson contraction in the growth direction (the observed interplanar spacing in AlN is smaller than in an unstrained state of AlN, where it is equal to 2.02 Å). Additionally, the measured d_{200} in CrN slightly oscillates, which also gives a hint about the actual strain state within the CrN layer.

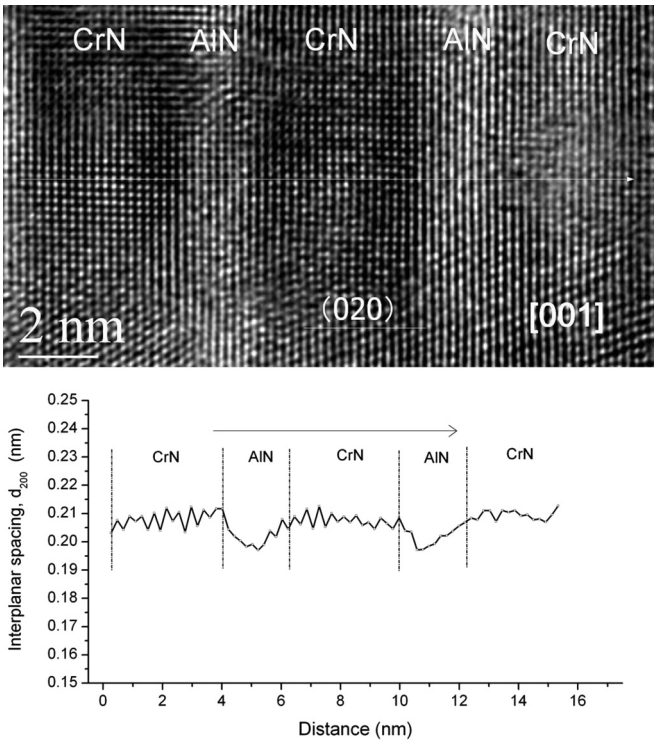

FIG. 1. Typical C_S-corrected HRTEM images (Wiener filtered) recorded along the [001] direction of the CrN/AlN multilayer films (upper), and corresponding d_{200} spacings (lower). Please note that bright and dark contrasts in the HRTEM image, together with the intensity profile, approximately correspond to the AlN and CrN layers, respectively. The arrow indicates the growth direction.

B. DFT calculations

Quantum-mechanical calculations using DFT were performed to verify the experimental observations. Three different supercells with different numbers of atoms, hence corresponding to different bilayer periods ($\Delta = 1.6$, 2.4, and 3.2 nm), were constructed for calculations. As an example of the used structural models, Fig. 2(b) depicts the $\Delta = 2.4$ nm supercell, while all the calculated interplanar distances are summarized in Fig. 2(a). The CrN layer exhibits a large spread of interplanar spacings while AlN yields almost a single-valued d_{002} spacing.

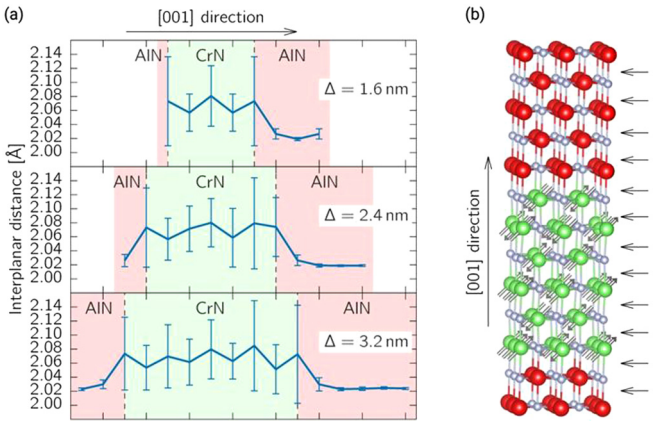

FIG. 2. (a) Calculated interplanar spacings in the multilayers with different bilayer periods ($\Delta = 1.6$, 2.4, and 3.2 nm) plotted against their position in the supercell. The oscillatory behavior clearly varies as a function of the bilayer period. (b) Atomic models for the 96-atom (3+3, $\Delta = 2.4$ nm) supercell. The small arrows on the right mark positions where the interplanar distances were measured [the bottom arrow corresponds to the leftmost data point in the middle panel of (a)]. Green, red, and gray spheres represent Cr, Al, and N atoms, respectively. The arrows on the Cr atoms represent the collinear spins distributed according to the special quasirandom structure (SQS) method.

The spread corresponds to a standard deviation obtained from measuring all interplanar distances (in the fully relaxed supercell) for a given pair of planes; the lateral size of the supercell implies in total eight independent columns, which are considered for the above-mentioned statistical analysis. The mean value for each pair of planes is shown by thick lines in Fig. 2(a). Interestingly, the mean value of the interplanar spacing exhibits oscillations in CrN while it is a constant in the AlN layer. Moreover, it is noted that the magnitude of oscillation is predicted to slightly change with the bilayer period, and it becomes reduced when the bilayer period increases above 2 nm. This is in excellent agreement with our experimental observations (Fig. 1). The minor difference between calculated and measured results may be attributed to the specific experimental conditions such as surface relaxation for a thin TEM sample, etc.

C. Electron-energy-loss spectroscopy analysis

The atomic displacements affect the electronic structure of the multilayers. EELS quantification and a fine-structure analysis further allow gaining insights into the electronic structure changes. High-spatial-resolution EELS measurements were further carried out on the multilayers with a bilayer period (Λ) of 2.0 and 5.5 nm. Compositional quantification using EELS reveals that Cr/N atomic ratios across the several layers (Fig. 3) periodically oscillate from CrN to AlN layers, which corresponds to the multilayer structure. It denotes that the atomic ratio changes in a different way for each bilayer period, a sharp change occurs for a small bilayer period while a more gradual change appears at the interface for a larger bilayer period. Given that the probe size is comparable to the layer thickness, the broadening of the intensity profiles

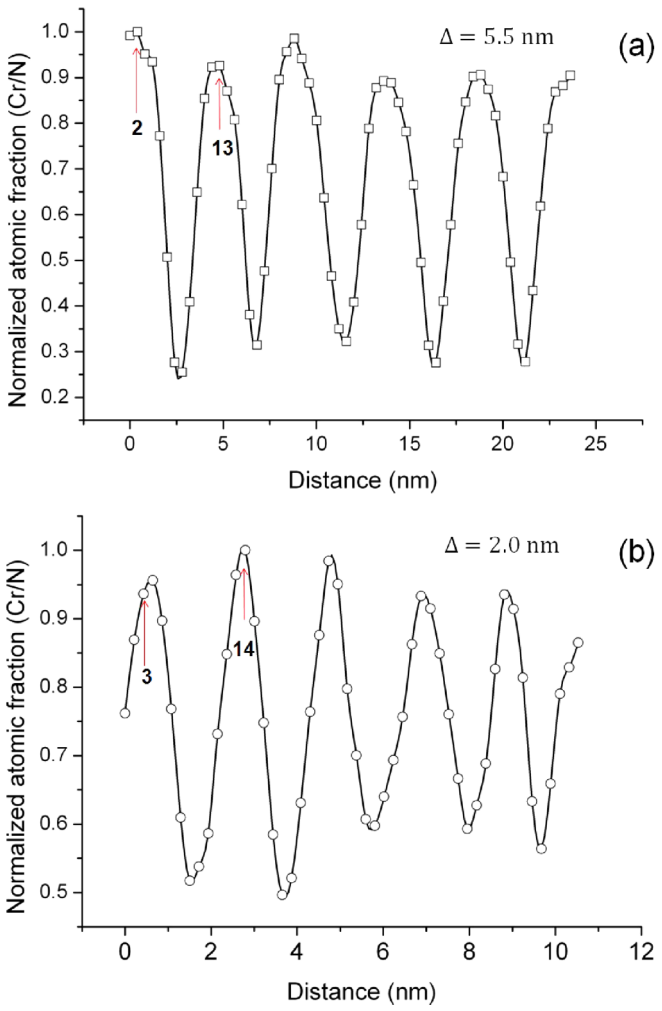

FIG. 3. Cr/N atomic ratio profiles for multilayer obtained by EELS line scan. It shows the chemical composition oscillations as a function of distance across the layers. (a) AlN 2.0 nm/CrN 3.5 nm ($\Lambda = 5.5$ nm); (b) AlN 1.0 nm/CrN 1.0 nm ($\Lambda = 2.0$ nm). Note that the indicated numbers are starting position and ending position for ELNES analysis (as shown in Fig. 5).

is at least partially caused by the instrumental resolution, apart from the interdiffusion-induced blurring across the interface. Obviously, it demonstrates that a certain amount of interdiffusion across the interface has occurred.

The strains can induce changes of the electronic structure [33], e.g., by modifying the bond length when subjected to a larger strain (smaller bilayer period). First, the L_3/L_2 ratios in the Cr-$L_{2,3}$ edge are evaluated (see Supplemental Material, Fig. 1S [34]) by fitting the $L3$ and $L2$ peaks using a step function [35]. It is found that the change of L_3/L_2 ratio with distances shows a similar behavior as the Cr/N atomic ratio. The L_3/L_2 ratio varies with the atomic ratio (or off stoichiometry) in CrN (Fig. 4), presenting as a clearly nonlinear trend. The depletion of Cr atoms in the entire volume leads to lowering of the L_3/L_2 ratio. On the other hand, a quantitative HRTEM strain analysis [36] indicates larger strain being present in the superlattice with a smaller bilayer period. Altogether it is noted that under the presence of a pronounced strain state (as in the case of a smaller bilayer period), the

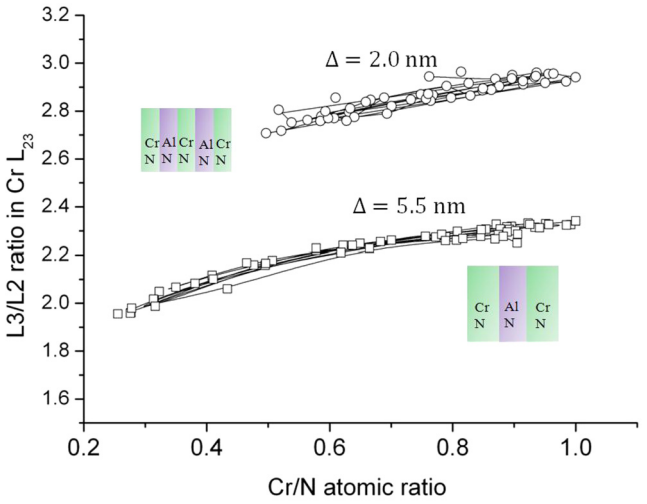

FIG. 4. L_3/L_2 ratio varies with the Cr/N ratio for a different bilayer period. The upper curve corresponds to AlN 1.0 nm/CrN 1.0 nm ($\Lambda = 2.0$ nm); the lower curve corresponds to the thickness: AlN 2.0 nm/CrN 3.5 nm ($\Lambda = 5.5$ nm). Schematic drawings of multilayer with distinct strain states inserted.

L_3/L_2 ratios are far larger than those measured under a smaller strain state (a larger bilayer period), the latter being in the range of ratio for transition metals [35,37], i.e., $L_3/L_2 \sim 2.2$. Experimentally, it qualitatively reveals how the strained multilayer affects the electronic structure in the CrN/AlN multilayer.

D. Electron-energy-loss near-edge structure

The fine structures of the N-K absorption edges (ELNES) in CrN are dissimilar under different strain conditions (Fig. 5). This is mainly reflected in a subtle difference of the first edge in the N-K edge. (i) The intensity of the N-K first edge at around 397 eV (indicated by an arrow) becomes significantly reduced under high strain state [smaller bilayer period, Fig. 5(b)] as compared to those under low strain state [larger bilayer period, Fig. 5(a)] at around 395 eV. (ii) N-K preedge suppression occurs not only in CrN, but also in AlN. (iii) The center of preedge of N-K periodically changes from AlN to CrN layer [similar periods as Figs. 3(a) and 3(b)], in the range of 395.2–394.6 eV (larger bilayer period) and 397.18–397.42 eV (smaller bilayer period). The second peak of N-K in CrN is also noticeably split into two peaks (a clear bump visible, indicated by short arrows) under a smaller bilayer period. The comparison of N-K edges reveals a clear shift toward a lower energy position in AlN than in CrN. The shift is also affected by strain states as will be demonstrated in the following section. These changes are closely relevant to changes of nitrogen orbitals when subjected to the different strained states.

Another generalized feature is the energy difference between Cr-$L_{2,3}$ and N-K edges caused by strains (Supplemental Material, Fig. 2S [34]), which are supposed to be relevant to the charge transfer from metal to nitrogen atom. It is noted that a larger strain applied to CrN enlarges the energy difference (up to 169.5–170.5 eV), varying

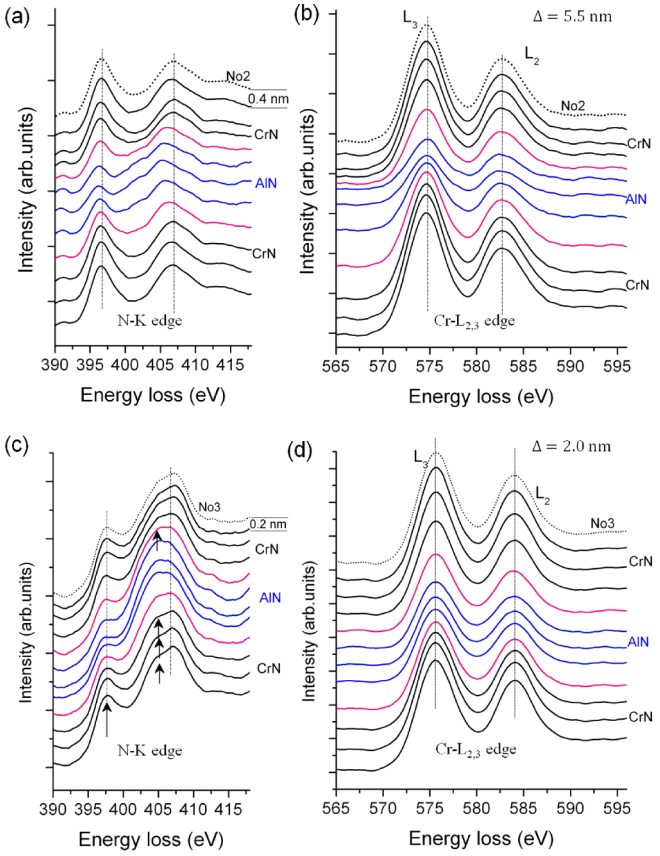

FIG. 5. (a) and (b) Fine-structure changes of N-K and Cr-$L_{2,3}$ edges when crossing the CrN and AlN layers for a large bilayer period ($\Lambda = 5.5$ nm), starting from spectra number 2 to 13 along the line where EELS line scan was performed [labeled in Fig. 3(a)]. (c) and (d) Fine-structure change of N-K and Cr-$L_{2,3}$ edges when crossing the CrN and AlN layers for a small bilayer period ($\Lambda = 2.0$ nm), starting from spectra number 3 to 14 [labeled in Fig. 3(b)]. The short dotted spectrum is a starting position, and red spectra are acquired from interface locations, blue spectra are obtained from AlN layer while the black spectra are from CrN. Please note the difference in the fine structures of N-K and Cr-$L_{2,3}$ edges at different locations and for different bilayer periods. Spectra in both cases are aligned in Cr-$L3$ (574.8 eV) for comparisons.

slightly with the Cr/N atomic ratio, whereas it is only about 167.5–169.5 eV for a smaller strain state (or a larger bilayer period). Similarly, the energy difference between L_2 and L_3 is increased up to 0.4 eV for a larger strain state, and solely 0.2 eV for a smaller strain state (shown in Fig. 2S [34]). In principle, the oscillations of the interplanar distance lead to changes in the electronic structure, and consequently variations of the N-K or Cr-$L_{2,3}$ edges. However, the subtle changes are hardly detectable with the current instrument used.

The strain in the growth direction (or perpendicular to the interfaces, e_{xx}) is tensile in CrN and compressive in AlN. In-plane strains are compressive in CrN and tensile in AlN, as suggested by the lattice parameters ($a_{\mathrm{CrN}} = 4.13$ Å, $a_{\mathrm{AlN}} = 4.07$ Å). Employing the strain maps [36] through HRTEM analysis and the fine structure of the Cr-$L_{2,3}$ edges, a relationship between the L_3/L_2 ratio and

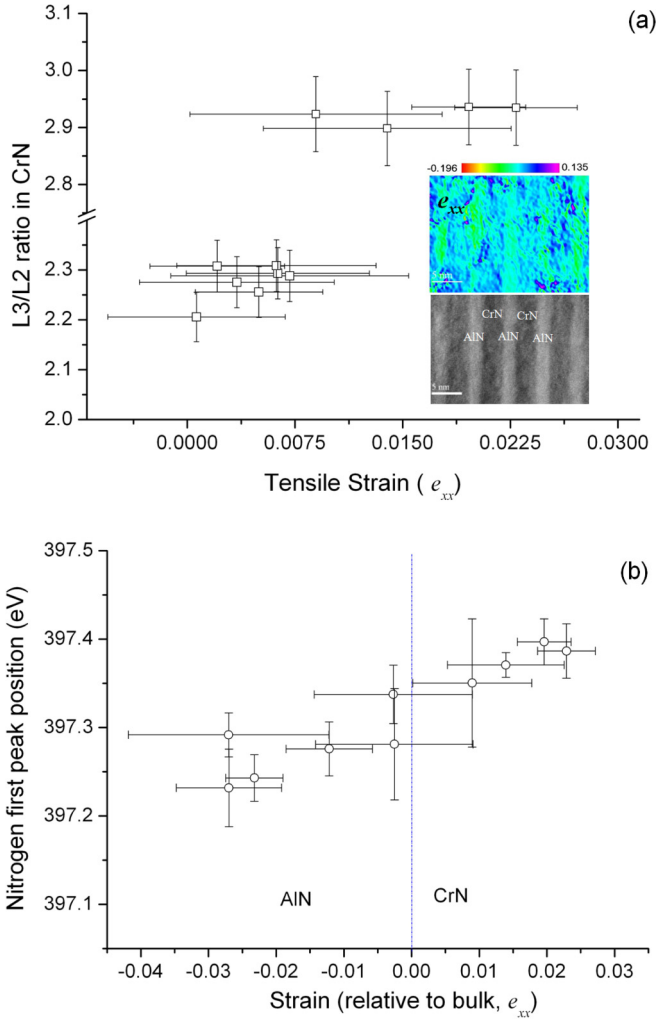

FIG. 6. (a) Relation of L_3/L_2 ratio and strains applied to the CrN layer. Insets are clippings of e_{xx} maps obtained by geometrical phase analysis and corresponding HRTEM images. (b) First peak position (using non-linear least squares fitting) in N- K edge versus strain. e_{xx} denotes the strain perpendicular to interface (along the growth direction).

strains can be quantitatively established [Fig. 6(a)]. It reveals that an increase of tensile strains in CrN results in an increase of the L_3/L_2 ratio. This effect is very significant, and when the tensile strain (e_{xx}) increases from 0.75% to 1.5%, the L_3/L_2 ratio rises from ∼2.3 up to ∼2.9. It experimentally demonstrates to what extent the strain can influence the electronic structure. We speculate that the origin of the L_3/L_2 ratio behavior is related to alternations of the first nearest-neighbor atomic surroundings actuated by constraints together with the number density of interfaces which is essentially related to the volume fraction of bulklike and interfacelike material. Together with Fig. 4, it clearly shows that the L_3/L_2 ratio is sensitive not only to the (non-)stoichiometry, but also to the actual strain state in CrN.

Strains can also trigger shifts of the N-*K*-edge peak [38]. A quantitative correlation of strains with the peak shifts is complicated. Alternating strain field within the CrN/AlN multilayer could be visualized using the geometrical phase analysis [cf. the inset in Fig. 6(a)] [36]. Combining strain maps obtained by quantitative HRTEM and EELS measurements enables detection of strain effects on the electronic structure. The change of the first peak position of the N-*K* edge with strain imposed on the nanolayer is shown in Fig. 6(b), and exhibits an approximately linear relation. The increase of tensile strains in CrN shifts the first peak to a high-energy position while the increase of the compressive strains in AlN shifts the peak to a lower-energy position. This is a first experimental report, directly linking the elastic strains to N-*K*-edge variations in CrN and AlN, which was allowed by combining high-quality EELS and HRTEM measurements, and a special sample architecture. In summary, strains sensitively affect not only the ELNES shapes (see Fig. 5) but also the peak positions.

E. Discussion

The origin of peculiar distribution of interplanar distances in CrN/AlN superlattices can be traced to their electronic structure and bonding. First, there are intrinsic differences in the dominant type of bonding in both materials. Two types of covalent bonds in CrN may be identified by inspecting the charge density of a planar cut through the $3 + 3(\Delta = 2.4\,\text{nm})$ superlattice shown in Fig. 7(a): charge in the ⟨100⟩ directions corresponds to the sp^2d^3 hybridized orbitals, similarly to other nitrides [31]. Additionally, charge accumulation in the ⟨110⟩ directions reflects the bonding interaction of Cr *d*-Cr *d* states. On the other hand, no such charge accumulation is obvious in AlN, where the *d* electrons are missing. The ionic bonding, related to the charge transfer from metal to nitrogen atoms, is visualized by the charge-difference map [Fig. 7(b)] which is the difference between actual charge density in CrN and a superposition of charges of isolated atoms. Clearly, there is a depletion of charge from the regions corresponding to metal atoms, and related charge accumulation at the nitrogen atoms, as suggested also by the electronegativity values: N: 3.0, Al: 1.5, Cr: 1.6. Charge-density difference integrated over the cross-sectional area is plotted as a function of the position in the [001] direction perpendicular to the interfaces in Fig. 3(c). While the interplanar space in AlN is depleted in charge which is transferred to the atomic planes, hence creating strong ionic bonds, the integrated charge difference in CrN exhibits shallow minima at the atomic planes (slight depletion of the charge) surrounded by maxima on both sides. These are related to the charge accumulation from the Cr *d*-Cr *d* bonds and have predominantly a metallic character resulting in a more compliant response to any perturbations. Interface is certainly a perturbation of the periodic crystal structure, hence causing Friedel oscillations of the charge density [39] which, in turn, lead to the oscillating interplanar distances. These oscillations get dumped toward the middle of the CrN layer, as is suggested also by Figs. 1 and 2. Finally we propose that no such interplanar oscillations appear in AlN due to the strong ionic bonds. On the other hand, as a consequence of these oscillations, decohesion and ideal shear do not occur within the interface, but in the region adjacent to the interface, i.e., in SiN-TiN composites, in the TiN slabs between the Ti-N planes parallel to that interface [40,41]. It is also expected that oscillations in the CrN-AlN multilayers could modify the shear of interface and fracture

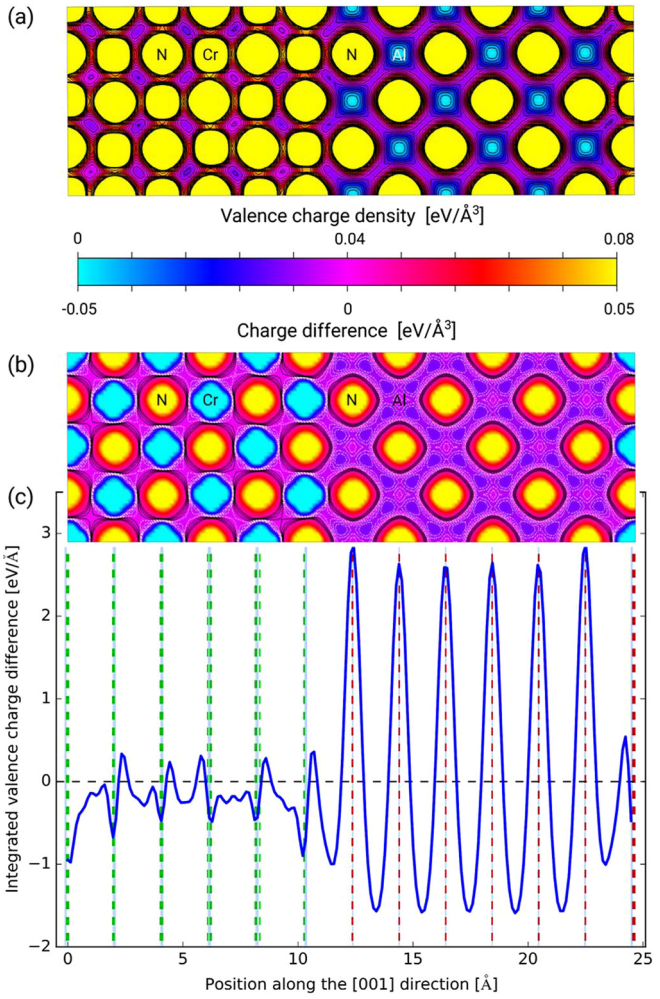

FIG. 7. Charge-density maps of the CrN/AlN 3+3 superlattice ($\Lambda = 2.4$ Å). (a) Valence charge density demonstrating the covalent Cr-N and Cr-Cr bonds in the CrN layer. (b) Charge-difference map with respect to overlapping atomic charges demonstrating the charge transfer from metal atoms to N. (c) Integrated charge difference from (b).

behaviors. Eventually, the hardness and other mechanical properties pertaining to the multilayers can be changed accordingly.

DFT calculations were also performed to corroborate the strain-induced effects on the electronic structure. Using the Slater transition-state approximation implemented via a partial core hole (pch) to calculate the N-K edge in cubic AlN in equilibrium and under two biaxial stress conditions [quantified by strain corresponding to e_{xx} in Fig. 6(b)], trends similar to the experimental observations were obtained. The relative edge onset [Fig. 8(b)] was estimated as the difference of energy of the initial core state ($1s$) in strained and unstrained states, assuming that the edge onset with respect to the Fermi level is the same in all considered strained states. This is supported by the overlap of the calculated N-K edges shown in Fig. 8(a). Indeed, in the state that AlN is when in the CrN/AlN superlattice, i.e., $a_x < a^{\mathrm{AlN}}$, i.e., $e_{xx} < 0$, the peak edge onset slightly decreases. The predicted rate, however, is much larger in comparison with the experimentally measured trends [Fig. 6(b)]. Despite this quantitative disagreement, we can qualitatively corroborate the experimentally observed shift of the N-K edge with the strain present in the sample.

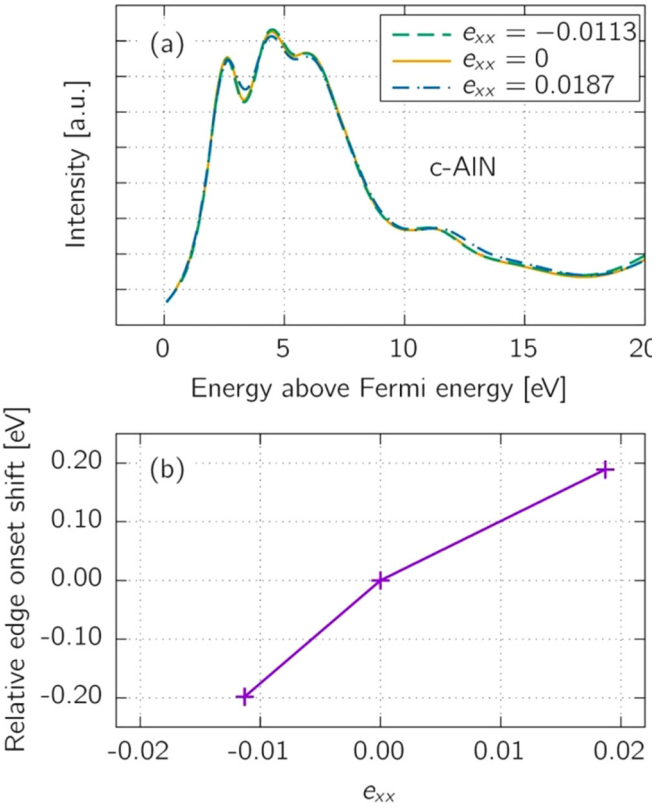

FIG. 8. (a) Calculated ELNES of c-AlN N-K edge under different strain states. (b) Plot of the relative onset of N-K edge in c-AlN with respect to unstrained state.

IV. CONCLUSIONS

To summarize, atomic displacement oscillations in the strained multilayers were observed, which are corroborated by DFT calculations. The oscillations are closely related to the charge redistributions. Strain states in the multilayers triggered by periodic chemical distribution lead to the fine-structure changes, such as the L_3/L_2 ratio, the peak shapes in N-K edges, and peak shifts, revealing the local variations in the electronic structure. In particular, the complex analysis enabled by combining HRTEM and EELS reveal dependence of the L_3/L_2 ratio and N-K-edge peak position on the local strain and chemical composition in the strained CrN/AlN multilayers, which are partially corroborated by the density functional theory calculations.

ACKNOWLEDGMENTS

We gratefully acknowledge Gabriele Moser and Herwig Felber at the Erich Schmid Institute of Materials Sciences, Austrian Academy of Sciences for their help with the TEM sample preparation and microscope operation. The computational results presented have been achieved using the Vienna Scientific Cluster (VSC).

[1] M. Stueber, H. Holleck, H. Leiste, K. Seemann, S. Ulrich, and C. Ziebert, J. Alloys Compd. **483**, 321 (2009).
[2] S. A. Barnett, Annu. Rev. Mater. Sci. **24**, 481 (1994).
[3] O. Knotek, F. Löffler, and G. Krämer, Surf. Coat. Technol. **54-55**, 241 (1992).
[4] H. Holleck and V. Schier, Surf. Coat. Technol. **76-77**, 328 (1995).
[5] S. J. Bull and A. M. Jones, Surf. Coat. Technol. **78**, 173 (1996).
[6] P. C. Yashar and W. D. Sproul, Vacuum **55**, 179 (1999).
[7] A. Inspektor and P. A. Salvador, Surf. Coat. Technol. **257**, 138 (2014).
[8] B. Saha, G. V. Naik, S. Saber, C. Akatay, E. A. Stach, V. M. Shalaev, A. Boltasseva, and T. D. Sands, Phys. Rev. B **90**, 125420 (2014).
[9] M. Friak, D. Tytko, D. Holec, P. P. Choi, P. Eisenlohr, D. Raabe, and J. Neugebauer, New J. Phys. **17**, 093004 (2015).
[10] V. Chawla, D. Holec, and P. H. Mayrhofer, J. Phys. D: Appl. Phys. **46**, 045305 (2013).
[11] M. Schlogl, B. Mayer, J. Paulitsch, and P. H. Mayrhofer, Thin Solid Films **545**, 375 (2013).
[12] A. Madan, I. W. Kim, S. C. Cheng, P. Yashar, V. P. Dravid, and S. A. Barnett, Phys. Rev. Lett. **78**, 1743 (1997).
[13] M. Setoyama, A. Nakayama, M. Tanaka, N. Kitagawa, and T. Nomura, Surf. Coat. Technol. **87**, 225 (1996).
[14] F. H. Mei, N. Shao, J. W. Dai, and G. Y. Li, Mater. Lett. **58**, 3477 (2004).
[15] J. Lin, J. J. Moore, B. Mishra, M. Pinkas, X. Zhang, and W. D. Sproul, Thin Solid Films **517**, 5798 (2009).
[16] D. Chen, X. L. Ma, and Y. M. Wang, Acta Mater. **53**, 5223 (2005).
[17] V. Chawla, D. Holec, and P. H. Mayrhofer, Thin Solid Films **565**, 94 (2014).
[18] D. A. Muller, Nat. Mater. **8**, 263 (2009).
[19] L. J. Allen, A. J. D'Alfonso, B. Freitag, and D. O. Klenov, MRS Bull. **37**, 47 (2012).
[20] R. Hahn, M. Bartosik, R. Soler, C. Kirchlechner, G. Dehm, and P. H. Mayrhofer, Scr. Mater. **124**, 67 (2016).
[21] M. Bartosik, J. Keckes, P. O. Å. Persson, H. Riedl, and P. H. Mayrhofer, Scr. Mater. **123**, 13 (2016).
[22] G. Kresse and J. Furthmüller, Comput. Mater. Sci. **6**, 15 (1996).
[23] G. Kresse and J. Furthmüller, Phys. Rev. B **54**, 11169 (1996).
[24] S.-H. Wei, L. G. Ferreira, J. E. Bernard, and A. Zunger, Phys. Rev. B **42**, 9622 (1990).
[25] L. Zhou, F. Körmann, D. Holec, M. Bartosik, B. Grabowski, J. Neugebauer, and P. H. Mayrhofer, Phys. Rev. B **90**, 184102 (2014).
[26] B. Alling, T. Marten, and I. A. Abrikosov, Phys. Rev. B **82**, 184430 (2010).
[27] J. P. Perdew, K. Burke, and M. Ernzerhof, Phys. Rev. Lett. **77**, 3865 (1996).
[28] G. Kresse and D. Joubert, Phys. Rev. B **59**, 1758 (1999).
[29] P. Blaha, K. Schwarz, P. Sorantin, and S. B. Trickey, Comput. Phys. Commun. **59**, 399 (1990).
[30] C. Hebert, Micron **38**, 12 (2007).
[31] D. Holec, R. Rachbauer, D. Kiener, P. D. Cherns, P. M. F. J. Costa, C. McAleese, P. H. Mayrhofer, and C. J. Humphreys, Phys. Rev. B **83**, 165122 (2011).
[32] K. Momma and F. Izumi, J. Appl. Crystallogr. **44**, 1272 (2011).
[33] V. J. Keast, M. J. Kappers, and C. J. Humphreys, J. Microsc. **210**, 89 (2003).
[34] See Supplemental Material at http://link.aps.org/supplemental/10.1103/PhysRevB.95.155305 for details, i) L_3/L_2 ratio versus the distances (different bilayer periods); ii) Cr/N atomic ratio versus energy difference between Cr-$L_{2,3}$ and N-K edge.
[35] D. H. Pearson, C. C. Ahn, and B. Fultz, Phys. Rev. B **47**, 8471 (1993).
[36] X. Gu, Z. L. Zhang, M. Bartosik, P. H. Mayrhofer, and H. Duan (unpublished).
[37] T. Riedl, T. Gemming, and K. Wetzig, Ultramicroscopy **106**, 284 (2006).
[38] M. Petrov, D. Holec, L. Lymperakis, J. Neugebauer, and C. J. Humphreys, J. Phys.: Conf. Ser. **326**, 012016 (2011).
[39] R. F. Zhang, A. S. Argon, and S. Veprek, Phys. Rev. Lett. **102**, 015503 (2009).
[40] S. Veprek, R. F. Zhang, M. G. J. Veprek-Heijman, S. H. Sheng, and A. S. Argon, Surf. Coat. Technol. **204**, 1898 (2010).
[41] R. F. Zhang, A. S. Argon, and S. Veprek, Phys. Rev. B **81**, 245418 (2010).